Invited Article: Comparison of hyperspectral coherent Raman scattering microscopies for biomedical applications

T. Bocklitz (iD), T. Meyer, M. Schmitt (iD), I. Rimke, F. Hoffmann, F. von Eggeling, G. Ernst, O. Guntinas-Lichius (iD), and J. Popp (iD)

COLLECTIONS

Paper published as part of the special topic on Biomedical Photonics and Coherent Raman Spectroscopy and Imaging

View Online   Export Citation   CrossMark

ARTICLES YOU MAY BE INTERESTED IN

Perspective: Coherent Raman scattering microscopy, the future is bright
APL Photonics **3**, 090901 (2018); https://doi.org/10.1063/1.5040101

Tutorial: Coherent Raman light matter interaction processes
APL Photonics **3**, 091101 (2018); https://doi.org/10.1063/1.5030335

Vibrational spectroscopy via stimulated Raman induced Kerr lensing
APL Photonics **3**, 092501 (2018); https://doi.org/10.1063/1.5029809

Invited Article: Comparison of hyperspectral coherent Raman scattering microscopies for biomedical applications

T. Bocklitz,[1,2,a,b] T. Meyer,[1,2,a] M. Schmitt,[1] I. Rimke,[3] F. Hoffmann,[4] F. von Eggeling,[1,4] G. Ernst,[2,4] O. Guntinas-Lichius,[4] and J. Popp[1,2]

[1]*Institute of Physical Chemistry and Abbe Center of Photonics, Friedrich Schiller University Jena, Helmholtzweg 4, 07743 Jena, Germany*

[2]*Leibniz Institute of Photonic Technology (IPHT), Member of Leibniz Health Technology, Albert-Einstein-Straße 9, 07745 Jena, Germany*

[3]*APE Angewandte Physik & Elektronik GmbH, Plauener Straße 163-165, 13053 Berlin, Germany*

[4]*Department of Otorhinolaryngology, Jena University Hospital, Haus A, Am Klinikum 1, 07747 Jena, Germany*

Raman scattering based imaging represents a very powerful optical tool for biomedical diagnostics. Different Raman signatures obtained by distinct tissue structures and disease induced changes provoke sophisticated analysis of the hyperspectral Raman datasets. While the analysis of linear Raman spectroscopic tissue data is quite established, the evaluation of hyperspectral nonlinear Raman data has not yet been evaluated in great detail. The two most common nonlinear Raman methods are CARS (coherent anti-Stokes Raman scattering) and SRS (stimulated Raman scattering) spectroscopy. Specifically the linear concentration dependence of SRS as compared to the quadratic dependence of CARS has fostered the application of SRS tissue imaging. Here, we applied spectral processing to hyperspectral SRS and CARS data for tissue characterization. We could demonstrate for the first time that similar cluster distributions can be obtained for multispectral CARS and SRS data but that clustering is based on different spectral features due to interference effects in CARS and the different concentration dependence of CARS and SRS. It is shown that a direct combination of CARS and SRS data does not improve the clustering results. © 2018 Author(s). *All article content, except where otherwise noted, is licensed under a Creative Commons Attribution (CC BY) license (http://creativecommons.org/licenses/by/4.0/).* https://doi.org/10.1063/1.5030159

Label-free imaging based on vibrational spectroscopy represents a powerful method to investigate the spatial distribution of various molecules in complex samples, particularly biomedical specimens.[1] A major advantage is the ability to visualize not only morphology but also molecular composition and function. Nowadays established vibrational imaging methods include spontaneous Raman scattering and IR absorption, which are, however, not suited for real time imaging of biological tissues. Spontaneous Raman scattering suffers from long acquisition times in the range of seconds and the frequent occurrence of a strong fluorescence background. IR imaging is limited by the water absorption and low spatial resolution, even though recent concepts have improved on the spatial resolution.[2] As an alternative, coherent Raman scattering (CRS) imaging has been used, but fastest implementations are based on imaging the distribution of a single vibrational Raman resonance only, instead of the full or a significant part of the vibrational spectrum, thereby significantly reducing the molecular information. This is due to the fact that changes in the spectral shape or shifts in the peak position cannot be extracted from few images but require spectral information. To overcome this limitation,

---

[a]T. Bocklitz and T. Meyer contributed equally to this work.

[b]Author to whom correspondence should be addressed: Thomas.Bocklitz@uni-jena.de

multiplex CRS[3] or hyperspectral coherent Raman imaging can be used. Multiplex CRS is conceptually very similar to spontaneous Raman spectroscopy requiring spectrographs and CCD detectors for data acquisition and data processing.[4,5] However, the acquisition time is significantly reduced to the ms range. Faster scanning can only be realized by hyperspectral CRS. Here, individual images are acquired at selected spectral positions and the laser source is tuned in between when recording the images.[6] As a third approach, simultaneous detection of a part of the spectrum within the CH stretching region has been employed using an array of tuned amplifiers (TAMP) and modulated broadband lasers.[7] The latter two techniques enable spectral scanning with μs integration time. Hence, hyperspectral CRS represents to date the fastest method for vibrational imaging, but so far little work has been reported on spectral processing of hyperspectral CRS data.[8]

Two CRS methods are nowadays established: coherent anti-Stokes Raman scattering (CARS) and stimulated Raman scattering (SRS). In multiplex CRS, primarily CARS has been applied so far, while SRS might be preferable in hyperspectral imaging. This shall be explained in the following based on Table I summarizing the different properties of CARS and SRS.

From Table I, it is evident that SRS has advantages in terms of molecular contrast and quantification as compared to CARS. In particular, SRS is linear in analyte concentration and the spectral lineshape is similar to spontaneous Raman scattering such that spectral data bases generated for spontaneous Raman data can be directly used for SRS. Due to the linear concentration dependence, SRS is more sensitive to dilute analytes, enabling the detection of molecular markers at lower concentrations in comparison to CARS. By contrast, interference of the CARS signal with the NRB results in distortions of the spectral line shape and shifts in the peak position requiring sophisticated algorithms like Kramers-Kronig or Maximum-Entropy and expensive calculations to extract the spontaneous Raman spectrum.[5] However, implementing CARS into standard laser scanning microscopes is more common since neither laser modulation of one of the lasers nor special detectors and sophisticated frequency-selective amplifiers like lock-in amplifiers (LIA) or tuned amplifiers (TAMP) are needed. Furthermore, the spatial resolution of CARS microscopy is potentially higher due to a higher-order nonlinear dependence on the excitation laser intensity and high resolution imaging schemes seem possible.[9]

The analysis of the multispectral Raman data of biological samples requires sophisticated data analysis, no matter if spontaneous or coherent Raman scattering is used.[10,11] This is due to the fact that differences in the concentration of marker molecules like protein, DNA, and lipids are rather small for different tissue types. Therefore, appropriate spectral pre-processing steps to correct for background signals and other illumination artefacts are needed.[10,12] In this contribution, we have simultaneously recorded hyperspectral CARS and SRS datasets for head and neck tissue samples, analyzed the datasets by multispectral data analysis approaches, and compared the results.

A biopsy of the floor of the mouth was used for the analysis as part of head and neck surgery. The tissue was composed of muscle, fat, and glands (Fig. 1). The tissue was analyzed by CARS and SRS within the CH stretching spectral region from 2650 to 3100 cm^{-1}.

TABLE I. Comparison of the properties of stimulated Raman scattering (SRS) and coherent anti-Stokes Raman scattering (CARS).

|	SRS	CARS
Concentration dependence	Linear	Linear to quadratic
Intensity dependence	~I (pump) I (Stokes)	~I^2 (pump) I (Stokes)
Background	Background free	Nonresonant background (NRB)
Spectral shape	As in spontaneous Raman	Spectral distortions due to interference with NRB
Peak position	As in spontaneous Raman	Shifted
Detector and amplifier	Photodiode and lock-in amplifier (LIA) or TAMP	PMT, standard amplifier, e.g., transimpedance amplifier
Modulation of laser	Yes	No
Laser noise	Highly problematic at the modulation frequency and shot to shot	Not specifically sensitive to laser noise
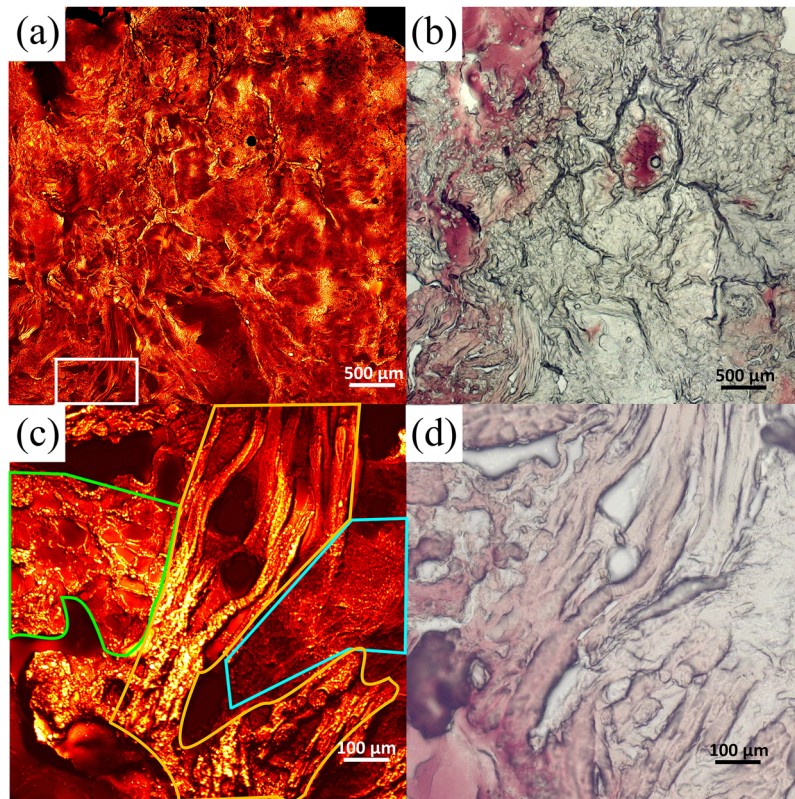
FIG. 1. Overview of tissue section. In panel (a), an overview CARS image of a human head and neck tissue section at the symmetric aliphatic CH stretching vibration of methylene groups CH_2 at 2850 cm^{-1} is shown. The image in panel (a) has been generated by combining single images and is compared to a whitelight image of the native tissue section under investigation shown in panel (b). The white marked area in the lower left corner of panel (a) is enlarged in panel (c). The whitelight images have been acquired using a Zeiss Axiovert 200M microscope and a 10× objective (Plan-Apo, Zeiss, Germany). The section is composed of glandular (blue line), muscle (yellow line), and adipose tissue (green line). In panels (c) and (d), CARS and whitelight images of the area marked in the lower left of panel (a) are displayed. This area has been investigated by hyperspectral CRS. CARS images were acquired using 23 mW of pump and 24 mW of Stokes power at the sample.

Coherent Raman imaging experiments have been performed using a compact fiber laser pumped optical parametric oscillator (OPO, picoEmerald S, APE, Berlin, Germany).[13] The OPO is pumped by the second harmonic of an Yb-fiber laser emitting pulses at 80 MHz pulse repetition rate of 2 ps duration and 1032 nm central wavelength. This laser is also used as the Stokes beam in the imaging experiments. The OPO generates a signal and idler of approximately >500 mW (signal 750-960 nm) and >400 mW (idler 1150-1350 nm) average power by parametric conversion, respectively. At approximately 800 nm signal wavelength as used in the experiments here, the laser provides typically 900 mW output power. The signal is tunable from 700 to 960 nm and used in the CRS imaging experiments as the pump beam such that CRS imaging from 720 to 4500 cm^{-1} can be realized. The laser provides electronic control of pulse overlap, wavelength tuning, and compensation of the walk-off of pump and Stokes beams resulting from microscope optics by a delay stage. An integrated electro-optic modulator is modulating the Yb-laser at 20 MHz for SRS. For CRS imaging, the laser was coupled into a home-built laser scanning microscope equipped with a 20× microscope objective (20× NIR Apo, NA = 0.4, Mitutoyo, Japan) imaging the sample using 47 mW laser power at the sample.[13,14] Both CARS and SRS signals are detected in the forward direction. A dichroic longpass beam splitter at 735 nm (Semrock, USA) separates SRS and CARS signals. The CARS signal is additionally filtered from residual laser light using a 770 nm short pass filter (Semrock, USA) and a bandpass filter at 650 nm (Thorlabs, USA). For SRS detection, two short pass filters (short pass 1000 nm Thorlabs, USA, short pass 1010 nm, Semrock, USA) are placed in front of a large area (10 mm^2) Si-photodiode connected to a fast analog LIA (APE, Berlin, Germany). The LIA operates

in the modulation frequency range from 8 to 20 MHz, providing −4.5 to 43.5 dB amplification and additional 12 dB post amplification at time constants as small as 100 ns.

For the CRS imaging experiments, a frozen human head and neck tissue section has been investigated by whitelight and CRS microscopy within the CH-stretching spectral region, as displayed in Fig. 1. In Fig. 1(a), an overview and in Fig. 1(c) a detailed CARS image at the symmetric aliphatic CH stretching vibration of methylene groups CH_2 at 2850 cm^{-1} are compared to the whitelight microscopic images of the same area displayed in Figs. 1(b) and 1(d). The area shown in Figs. 1(c) and 1(d) has been investigated by simultaneously detecting hyperspectral CARS and SRS from 2650 to 3100 cm^{-1} by tuning the pump laser from 782 nm to 810 nm in steps of 1 nm. This step corresponds to approximately 15 cm^{-1}. For imaging, 23 mW of pump and 24 mW of Stokes laser power have been used at the sample. The area shown in Figs. 1(c), 2, and 3 is composed of glandular, adipose, and muscle tissues, as indicated. The data analysis on the hyperspectral image stacks was performed using the free programming environment R.[15] The applied analysis pipeline started by
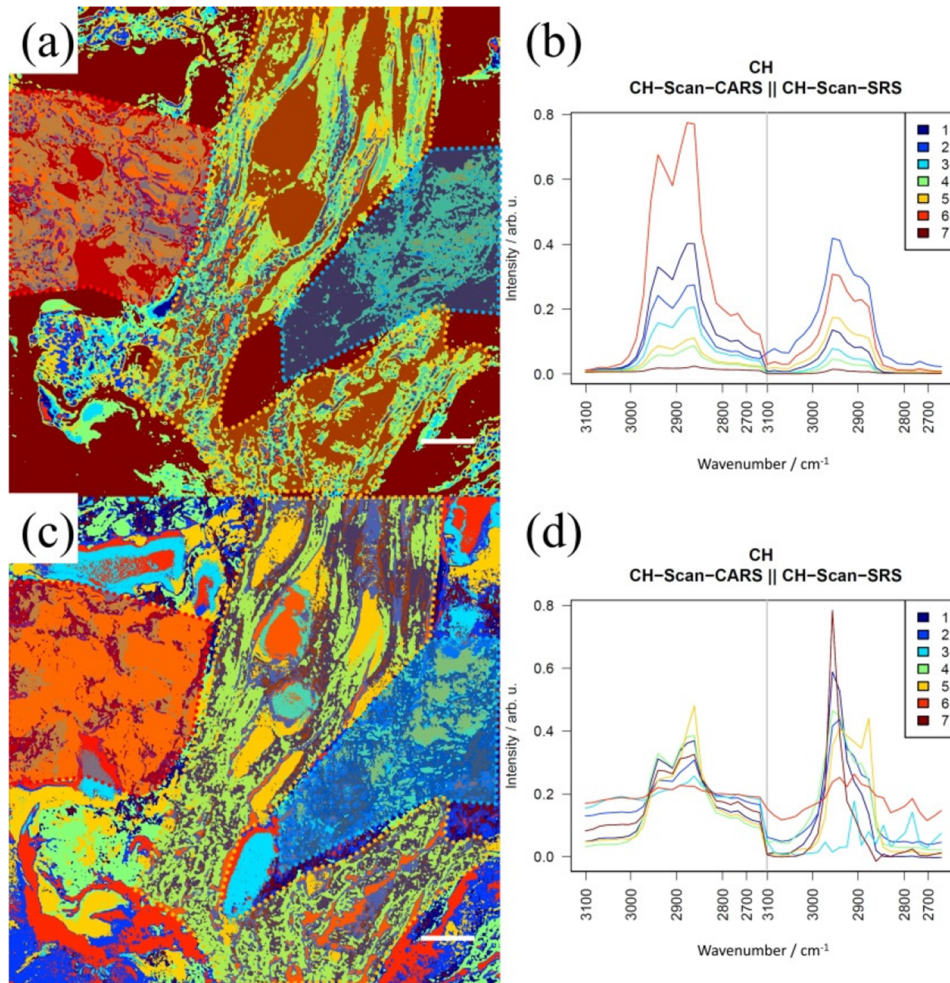
FIG. 2. Cluster analysis result for the combined SRS-CARS data. The combined SRS-CARS data stack was utilized for a k-means cluster analysis. The cluster distribution based on un-normalized data is shown in (a), while the corresponding mean spectra are visualized in (b). In a similar manner, panel (c) shows the cluster distribution of a k-means cluster analysis of the normalized spectra with corresponding mean spectra (d). The different tissue types within the section are indicated in panels (a) and (c), i.e., glandular (blue area on the right), muscle (yellow area in the centre), and adipose tissues (red area on the left). The clusters do not represent the tissue types in case of (a). Normalization improves the classification of the different tissue types, as evident from panel (c). In general, however, the distribution of CARS and SRS signals is not co-localized. This can be seen that the cluster mean spectra do not show a similar behavior in the CARS and SRS part. Scale bar 100 μm.
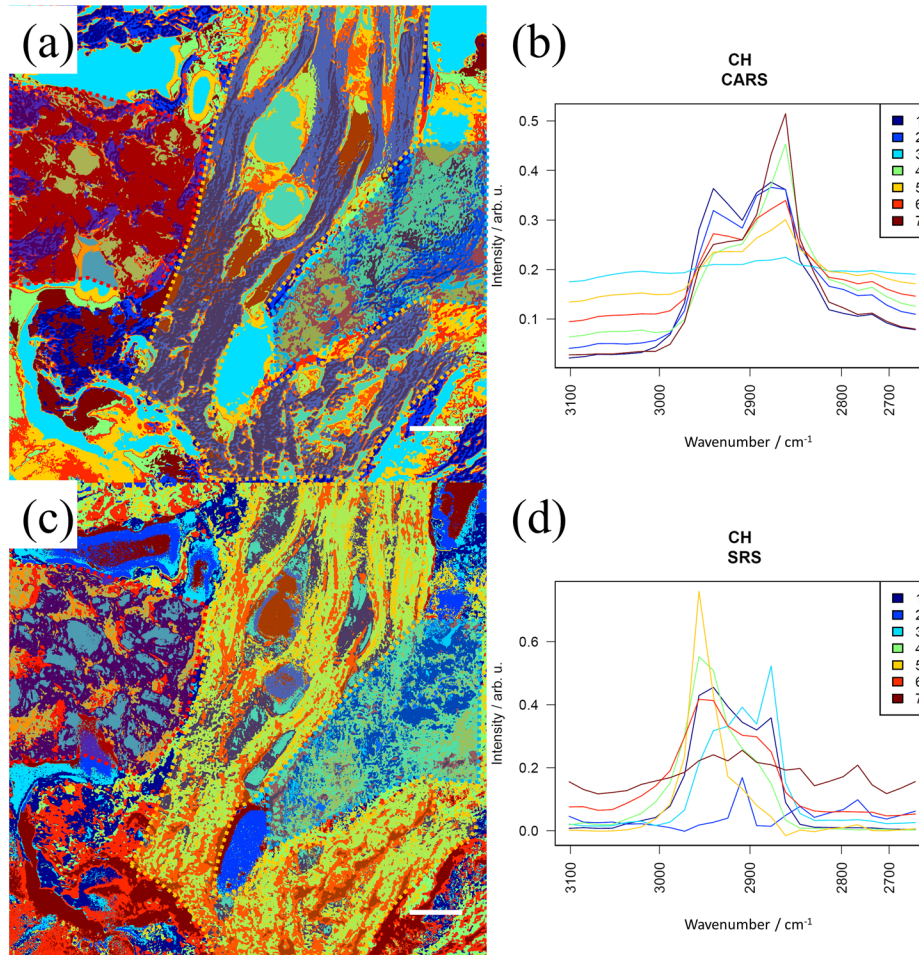
FIG. 3. Cluster analysis result for the SRS and CARS data separately. The CARS-SRS data stack was separately analyzed using a k-means cluster analysis. The cluster distribution based on normalized CARS data is shown in (a), while the cluster distribution of normalized SRS data is shown in (c). The different tissue types within the section are indicated in panels (a) and (c), i.e., glandular (blue area on the right), muscle (yellow area in the centre), and adipose tissues (red area on the left). The corresponding mean spectra are shown in panels (b) and (d). Even though all cluster means show different contributions within the wavenumber region, the cluster distribution can be used for imaging purposes in both cases (SRS and CARS), as the same tissue structures (glandular, muscle, and adipose tissues) are visible and distinguishable in both plots (a/c). Scale bar 100 μm.

importing the respective images into R and re-arranging the SRS and CARS image data stacks. Both image stacks (CARS, SRS) featured 25 measurement channels. Every image of the image stack was median-filtered with a window size of 5. The stacks were afterwards combined, a principal component analysis (PCA) based dimension reduction was applied, and a k-means cluster analysis was performed using the PC scores of the combined data. The free parameter k was set to 7 in order to recover an overview of tissue structures. The CARS and SRS spectra in the respective stack were also vector normalized and thereafter combined. The same k-means cluster analysis was performed with k = 7 for the combination of the normalized data. To speed up the k-means optimization while retaining the optimum, we utilized a dimension reduction with only 8 PC-scores. This PC dimension accounted for 99.65% (raw and combined data), 96.72% (normalized and combined data), 99.85% (normalized CARS data), and 95.77% (normalize SRS data) of the cumulative variance within the respective data stack.

In Fig. 2, the results from a cluster analysis performed for the combined SRS-CARS data stacks are shown for normalized and non-normalized data. In Figs. 2(a) and 2(c), the cluster distribution is displayed, while panels (b) and (d) visualize the corresponding cluster mean spectra, which are

composed of a CARS spectral part and a SRS spectral part. In this manner, local differences between CARS and SRS spectra in terms of spectral shape and peak position can be interpreted. In Fig. 2(b), the mean spectra of the 7 clusters are displayed. It is evident that areas with highest CARS intensity do not correspond to areas of highest SRS signals; hence, CARS and SRS signals are not colocalized. Cluster 5 is characterized by the largest CARS signal, while the largest SRS signal is in cluster 2. This finding on non-normalized data is due to the fact that CARS signal intensity and SRS signal intensity have different concentration dependencies, as summarized in Table I. CARS is focusing on highly concentrated species due to the non-linear dependency on the concentration, while SRS features a linear concentration dependency. But other effects also play a role, e.g., the collection of SRS and CARS signals differs due to different signal wavelengths. In order to exclude such focusing differences of CARS and SRS, the normalized data were analyzed in the same manner, yielding a similar conclusion: The SRS spectra and CARS spectra of the same tissue regions are not identical. It can also clearly be seen that the ordering of signal peak intensities differs for CARS and SRS mean spectra of the 7 clusters. Due to the linear concentration dependence, SRS is more sensitive to molecules in lower concentration, while CARS provides better discrimination of abundant molecules and highlights areas of high concentration. Without normalization, however, very little information on different tissue structures can be extracted. Cluster 7 of the non-normalized data primarily corresponds not only to background areas, i.e., voids in the tissue, but also to areas of overall low concentration. The other clusters are well mixed and do not correlate with specific structures, e.g. adipocytes, muscle bundles, and glandular tissue [Fig. 2(a)].

This is due to the fact that the cluster distribution of the non-normalized data is highly dependent on the absolute signal intensity, which varies with the tissue thickness and the detection efficiency rather than changes in the composition. Therefore the same analysis has been performed for normalized SRS and CARS data. The results are displayed in Figs. 2(c) and 2(d). It is evident that the cluster distribution is different if normalized or non-normalized data are used. After normalization, two clusters 3 and 6 represent the background areas, but the area fraction of these clusters is smaller than that of cluster 7 in Fig. 2(a). Furthermore, the other clusters correlate in comparison to Fig. 2(a) to a higher extent with specific tissue structures, e.g., cluster 5 corresponds to adipocyte tissue and is characterized by highest CARS signal intensity. Cluster 4 and parts of cluster 1 and 2 primarily correspond to muscle bundles and those of cluster 1 and 7 correspond to the glandular tissue. However, also for normalized CRS data, the ordering of the relative CARS and SRS intensities for the 7 clusters differs. This might result in worse separation of tissue structures because the clustering is also based on differences in the normalized spectral intensity and peak position, which is different for CARS and SRS.

In order to exploit the information content within the SRS and CARS-stacks, the cluster analysis for both stacks has been performed separately using normalized data only in order to investigate whether tissue characterization can be improved in comparison to combined hyperspectral CARS and SRS imaging. In addition, the performance of both techniques for tissue characterization is investigated individually.

The results are displayed in Fig. 3. In Figs. 3(a) and 3(b), the cluster distribution and the cluster mean spectra of the hyperspectral CARS image stack are displayed, while panels (c) and (d) visualize the cluster distribution and mean spectra of the SRS spectral part. As evident when comparing Figs. 2(a) and 2(c) with Figs. 3(a) and 3(c), using SRS or CARS individually improves the discrimination of glandular, adipose, and muscle tissues. Cluster 7 in Fig. 3(a) corresponds to adipocytes and is characterized by the highest CARS intensity at 2850 cm^{-1}, while clusters 1 and 2 correspond to muscle fibers, which are spectrally characterized by similar CARS intensities at 2850 and 2930 cm^{-1}. Cluster 3 of low spectral differences represents the background, and the remaining clusters 4 to 6 are more abundant within the glandular tissue. In comparison to Fig. 2(c), tissue characterization is significantly improved for using normalized CARS spectra only. In Fig. 3(c), the same analysis has been performed on hyperspectral SRS data. Here, clusters 4 and 5 are characterized by the mean spectra of the highest signal intensity around 2960 cm^{-1} specifically highlighting muscle fibers, while clusters 1 and 3 are characterized by an additional peak at 2850 cm^{-1}, characteristic for CH$_2$ groups within adipocytes. The glandular tissue is mainly assigned to clusters 4 and 5, similar to the muscle tissue. When comparing the clustering results for CARS and SRS separately in Figs. 3(a) and 3(c), some

differences are apparent: first, the clusters obtained from hyperspectral CARS data are more uniform, enabling clear differentiation of adipose, muscle, and glandular tissues. Second, CARS is specifically sensitive to lipid-rich structures like adipocytes due to the quadratic concentration dependency on the scattering functional group CH_2. SRS on the other hand provides more spectral differences when comparing Figs. 3(b) and 3(d), but clustering of the different tissue types is slightly worse. This finding can be attributed to the fact that the concentration dependence of CARS and SRS signals is different; hence, the cluster distribution and the mean spectra do not coincide.

In summary, both CARS and SRS are suited for tissue characterization using hyperspectral coherent Raman imaging in combination with data processing. Combining CARS and SRS hyperspectral data into a single data stack does not improve clustering results due to the differences in the concentration dependence and the spectral peak position. Cluster analysis based on non-normalized data shows that the absolute signal is the dominating factor for characterization but is insensitive to specific tissue structures. This is due to the fact that the absolute signal intensity is highly dependent on experimental factors. Hence, spectral preprocessing, i.e., vector normalization of the data, is needed to improve characterization performance. For normalized data, the clustering results for different tissue structures improve; however, using CARS and SRS in combination provides worse structure characterization in comparison to analyzing normalized SRS and CARS data separately. This is due to the fact that the concentration dependence, the peak position, and the spectral profile differ for CARS and SRS such that interpretation is more ambiguous for the combined hyperspectral data sets than for the individual hyperspectral data sets. The cluster mean spectra indicate that the clustering of CARS data is highly dependent on the symmetric CH stretch vibration of methylene groups at 2850 cm^{-1}, while SRS clustering strongly depends on the vibrational bands at 2950 cm^{-1}. This indicates that CARS is very sensitive to lipids, while SRS provides better detection of DNA and protein, which are detected at 2930 and 2967 cm^{-1}.[16]

The reason for that is again the different concentration dependency of CARS and SRS and in addition the changes in the peak position due to interference with the nonresonant background. Therefore, the CRS imaging modality should be selected based on the species or molecules, their specific structure, and the concentration range of interest. Hence, for concentrated lipids, e.g., in lipid droplets, which are composed of fatty acids with long hydrocarbon chains with repetitive methylene groups, such that a single molecule like palmitic acid contains 14 methylene groups, CARS provides very high signals. Furthermore, integration of CARS imaging into standard LSM platforms is also much simpler than in the case of SRS: no laser modulation is needed, laser noise is less critical, and no lock-in or tuned amplifier or additional large dynamic range photodiode detector is needed. Furthermore, CARS provides higher spatial resolution due to the higher order nonlinearity. However, for molecules at lower concentrations and for imaging less abundant functional groups, SRS is more sensitive. It is demonstrated that data processing is needed for tissue characterization based on hyperspectral CRS. Concentrations of marker molecules are not extracted by the methods presented herein, and no semantic segmentation was carried out. This will be performed in further research, where a clinical question will be solved with one or both of the presented imaging methods. Nevertheless, it has been demonstrated that discrimination of specific tissue structures can be performed with SRS and CARS at similar quality, but both techniques focus on low or highly concentrated species, respectively.

[1] C. Krafft, M. Schmitt, I. W. Schie, D. Cialla-May, C. Matthaus, T. Bocklitz, and J. Popp, Angew. Chem., Int. Ed. **56**(16), 4392 (2017); C. Krafft, I. W. Schie, T. Meyer, M. Schmitt, and J. Popp, Chem. Soc. Rev. **45**(7), 1819 (2016).

[2] Y. Bai, D. Zhang, C. Li, C. Liu, and J.-X. Cheng, J. Phys. Chem. B **121**(44), 010249 (2017).

[3] C. H. Camp, Jr., Y. J. Lee, J. M. Heddleston, C. M. Hartshorn, A. R. H. Walker, J. N. Rich, J. D. Lathia, and M. T. Cicerone, Nat Photonics **8**(8), 627 (2014).

[4] Y. Liu, Y. J. Lee, and M. T. Cicerone, Opt. Lett. **34**(9), 1363 (2009); E. M. Vartiainen, H. A. Rinia, M. Müller, and M. Bonn, Opt. Express **14**(8), 3622 (2006).

[5] M. T. Cicerone, K. A. Aamer, Y. J. Lee, and E. Vartiainen, J. Raman Spectrosc. **43**(5), 637 (2012).

[6] Y. Ozeki, W. Umemura, Y. Otsuka, S. Satoh, H. Hashimoto, K. Sumimura, N. Nishizawa, K. Fukui, and K. Itoh, Nat. Photonics **6**(12), 845 (2012).

[7] C.-S. Liao, M. N. Slipchenko, P. Wang, J. Li, S.-Y. Lee, R. A. Oglesbee, and J.-X. Cheng, Light: Sci. Appl. **4**, e265 (2015).

[8] D. Fu and X. S. Xie, Anal. Chem. **86**(9), 4115 (2014); C.-Y. Lin, J. L. Suhalim, C. L. Nien, M. D. Miljković, M. Diem, J. V. Jester, and E. O. Potma, J. Biomed. Opt. **16**(2), 021104 (2011); J. L. Suhalim, C.-Y. Chung, M. B. Lilledahl, R. S. Lim, M. Levi, B. J. Tromberg, and E. O. Potma, Biophys. J. **102**(8), 1988 (2012); Y. Otsuka, K. Makara, S. Satoh, H. Hashimoto, and Y. Ozeki, Analyst **140**(9), 2984 (2015); S. Satoh, Y. Otsuka, Y. Ozeki, K. Itoh, A. Hashiguchi, K. Yamazaki, H. Hashimoto, and M. Sakamoto, Pathol. Int. **64**(10), 518 (2014).

[9] C. Cleff, P. Groß, C. Fallnich, H. L. Offerhaus, J. L. Herek, K. Kruse, W. P. Beeker, C. J. Lee, and K.-J. Boller, Phys. Rev. A **86**(2), 023825 (2012).

[10] S. Guo, S. Pfeifenbring, T. Meyer, G. Ernst, F. von Eggeling, V. Maio, D. Massi, R. Cicchi, F. S. Pavone, J. Popp, and T. Bocklitz, J. Chemom. **32**, e2963 (2017).

[11] C. Pohling, T. Bocklitz, A. S. Duarte, C. Emmanuello, M. S. Ishikawa, B. Dietzeck, T. Buckup, O. Uckermann, G. Schackert, M. Kirsch, M. Schmitt, J. Popp, and M. Motzkus, J. Biomed. Opt. **22**, 22 (2017); N. Vogler, T. Bocklitz, M. Mariani, V. Deckert, A. Markova, P. Schelkens, P. Rösch, D. Akimov, B. Dietzek, and J. Popp, J. Opt. Soc. Am. B. **27**, 1361 (2010).

[12] O. Chernavskaia, S. Guo, T. Meyer, N. Vogler, D. Akimov, S. Heuke, R. Heintzmann, T. Bocklitz, and J. Popp, J. Chemom. **31**(6), e2901 (2017).

[13] C. Stiebing, T. Meyer, I. Rimke, C. Matthäus, M. Schmitt, S. Lorkowski, and J. Popp, J. Biophotonics **10**(9), 1217 (2017).

[14] T. Meyer, M. Baumgartl, T. Gottschall, T. Pascher, A. Wuttig, C. Matthaeus, B. F. M. Romeike, B. R. Brehm, J. Limpert, A. Tuennermann, O. Guntinas-Lichius, B. Dietzek, M. Schmitt, and J. Popp, Analyst **138**(14), 4048 (2013).

[15] R Development Core Team, *R: A Language and Environment for Statistical Computing* (R Foundation for Statistical Computing, Vienna, Austria, 2008).

[16] F.-K. Lu, S. Basu, V. Igras, M. P. Hoang, M. Ji, D. Fu, G. R. Holtom, V. A. Neel, C. W. Freudiger, D. E. Fisher, and X. Sunney Xie, Proc. Natl. Acad. Sci. U. S. A. **112**(37), 011624 (2015).